


Restricted multicanonical sampling for machine learning potential constructionKazutoshi Miwa ^{*}*Toyota Central R&D Labs., Inc., Nagakute, Aichi 480-1192, Japan*

(Received 24 October 2022; revised 15 February 2023; accepted 16 February 2023; published 28 February 2023)

The restricted multicanonical (rMUCA) ensemble method is developed and combined with the on-the-fly machine learning potential (MLP) generation scheme. The rMUCA simulation performs a random walk in the potential-energy subspace restricted by the selected collective variables and allows us to sample physically relevant configurations without being trapped in local energy minima. No preliminary simulation runs are required to construct a bias potential. The sample structures for training are collected dynamically from the simulations using the MLP itself where the simultaneous error estimation is utilized to judge whether an updated structure should be added to the sample data set or not. The rMUCA formula can be also used for the saddle-point search with minor modification. The method is applied to the oxidation of carbon monoxide on platinum surfaces. The results show that the rMUCA simulation provides an efficient and accurate way to sample rare events for the MLP construction.

DOI: [10.1103/PhysRevB.107.054313](https://doi.org/10.1103/PhysRevB.107.054313)**I. INTRODUCTION**

Atomistic simulations, such as molecular dynamics (MD) and Monte Carlo (MC) methods are nowadays indispensable tools for investigating a wide variety of material properties [1,2]. Various ensemble techniques were developed to take desired statistics with isothermal and/or isobaric conditions [3–10]. The simulations in these physical ensembles, however, tend to get trapped in local minima on the potential-energy surface. If the energy minimum is surrounded by the barriers much higher than the thermal energy, only rare fluctuations can allow the system to jump over the barrier and move to a new minimum. Therefore, it is often difficult to directly simulate the transitions between two local-minimum states by the physical ensemble simulations due to their limited accessible timescales. To overcome this difficulty, the multicanonical (MUCA) and multibaric (MUBA) ensemble methods were proposed [11–18]. The MUCA ensemble is designed to realize a random walk in the potential-energy space. Similarly, the MUBA simulation performs a random walk in the volume space. These random walks are realized by introducing bias potentials which are usually constructed with preliminary simulation runs. In the MUCA (MUBA) ensemble simulation, the system explores the potential-energy surface over a wide range of temperatures (pressures) without being trapped in local energy minima.

In atomistic simulations, the accuracy of the interatomic potentials is an important issue. First-principles calculations based on density functional theory (DFT) [19–21] provide an accurate way to describe the atomic interactions with the quantum-mechanical treatment. Owing to high computational demands of DFT calculations, empirical interatomic potentials also are used, particularly, in large-scale simula-

tions. Since the accuracy of these potentials strongly depends on assumed functions and their parameters, much attention should be taken to determine them. An alternative approach to perform large-scale simulations is the machine learning potentials (MLPs) [22–25]. In the MLP, the total energy of a system is expressed by simple and flexible functions which are chosen from a mathematical viewpoint rather than physical motivation. Different types of bonding can be treated on the same footing. Since the MLP is a data-driven approach, how to select the sample data set for training is crucial. We have developed the automatic MLP generation scheme, self-learning and adaptive database (SLAD) [26] in which the sample structures are dynamically collected by MD simulations using the MLP itself. The simultaneous error estimation is utilized to judge whether an updated structure should be added to the sample data set or not. The expensive DFT calculations need to be performed only for the collected sample structures. The SLAD has been applied to various materials [26–29], demonstrating high computational efficiency with accuracy comparable to DFT calculations.

To generate the MLP applicable to the rare events, such as chemical reactions and structural phase transitions, the structure sampling should be carried out with the enhanced ensemble to favor the transitions between the states separated by energy barriers. In this context, we have recently combined the SLAD approach with the MUBA ensemble simulation to generate the MLP for predicting the phase stability under various pressures [18]. The advantage of our method is that the explicit construction of a bias potential is not required. This feature is essential to apply the MUBA simulation to the on-the-fly MLP generation.

In this paper, we present the SLAD approach combined with the MUCA ensemble to simulate chemical reactions. The random walk is realized in the potential-energy subspace restricted by selected collective variables. Hereafter, it is referred to as the restricted MUCA (rMUCA) method, which

^{*}miwa@cmp.tytlabs.co.jp

is designed to be free from the preliminary simulation runs to construct the bias potential as in the previous MUBA simulation. The rMUCA formula can be also utilized for the saddle-point search with minor modification. The utility of the method is demonstrated for the oxidation of carbon monoxide (CO) on platinum (Pt) surfaces.

The rest of this paper is organized as follows: In Sec. II, we describe the formalism for the rMUCA simulation and the related methods. In Sec. III, the results for the CO oxidation reactions on the Pt surfaces are presented, and the accuracy of the constructed MLP is examined. Section IV summarizes the main results of this paper.

II. METHODOLOGY

A. Restricted multicanonical simulation

The simulations are carried out with the hybrid Monte Carlo (HMC) method [30]. In the HMC method, the conventional canonical (NVT) ensemble is sampled using the microcanonical (NVE) Hamiltonian,

$$\mathcal{H}_{NVE} = \sum_i \frac{\mathbf{p}_i \cdot \mathbf{p}_i}{2m_i} + U(\{\mathbf{r}_i\}), \quad (1)$$

where \mathbf{r}_i ($i = 1, \dots, N$) represent atomic positions, \mathbf{p}_i are the momenta conjugate to \mathbf{r}_i , m_i are atomic masses, and U is the interatomic potential. The NVT sampling with the HMC is carried out as follows: (i) For a given atomic configuration, \mathbf{p}_i are refreshed by the Maxwell distribution. (ii) The microcanonical MD run is executed with a few time steps. (iii) The Metropolis criterion is applied for the change in the Hamiltonian $\Delta\mathcal{H}_{NVE}$ due to the configuration update to accept or reject the trial configuration. The acceptance probability is given by

$$p = \min[1, \exp(-\beta \Delta\mathcal{H}_{NVE})], \quad (2)$$

where $\beta (= \frac{1}{k_B T})$ is the inverse temperature. The HMC method combines the advantages of the MD and MC simulations, which allows the global MD configuration updates and does not suffer from the discretization error due to a finite time-step size [30].

In order to realize a random walk in the potential-energy space with the HMC, we introduce collective variables (CVs), c_j ($j = 1, \dots, N_c$) [31], and add a bias potential δU to \mathcal{H}_{NVE} ,

$$\mathcal{H}_{\text{rMUCA}} = \mathcal{H}_{NVE} + \delta U(\{c_j\}). \quad (3)$$

The variables $\{c_j\}$ are a small set of functions of \mathbf{r}_i ($N_c \ll N$) and map the entire degrees of freedom of the system into a reduced subspace. They should, therefore, be chosen properly to characterize the reaction process. Let us decompose the atomic force $\mathbf{F}_i (= -\frac{\partial U}{\partial \mathbf{r}_i})$ into the components parallel and perpendicular to this subspace. The parallel component is given by

$$\mathbf{F}_i^{\parallel} = \sum_j (\hat{\mathbf{n}}_i^j \cdot \mathbf{F}_i) \hat{\mathbf{n}}_i^j, \quad (4)$$

where $\hat{\mathbf{n}}_i^j$'s are orthonormal vectors ($\sum_i \hat{\mathbf{n}}_i^j \cdot \hat{\mathbf{n}}_i^k = \delta_{jk}$) which are obtained by applying the Gram-Schmidt procedure to $\mathbf{n}_i^j = \frac{\partial c_j}{\partial \mathbf{r}_i}$. The perpendicular component is given by $\mathbf{F}_i^{\perp} = \mathbf{F}_i - \mathbf{F}_i^{\parallel}$. If removing the parallel component \mathbf{F}_i^{\parallel} from the

real force \mathbf{F}_i in the dynamics of the MD updates, the system performs a random walk within the subspace restricted by the CVs. This is achieved by setting the bias potential to

$$\delta U = \sum_i (\mathbf{r}_i - \mathbf{r}_i^0) \cdot \mathbf{F}_i^{\parallel}(\{\mathbf{r}_i^0\}), \quad (5)$$

where \mathbf{r}_i^0 's denote the initial atomic positions for each HMC sweep. The corresponding derivative of the Hamiltonian is obtained as $\frac{\partial \mathcal{H}_{\text{rMUCA}}}{\partial \mathbf{r}_i} = -\mathbf{F}_i(\{\mathbf{r}_i\}) + \mathbf{F}_i^{\parallel}(\{\mathbf{r}_i^0\})$ that becomes approximately $-\mathbf{F}_i^{\perp}(\{\mathbf{r}_i\})$. The HMC simulation using $\mathcal{H}_{\text{rMUCA}}$ with Eq. (5), therefore, realizes the rMUCA sampling.

The advantage of the present method is that any preliminary simulation runs are not required to construct the bias potential. The bias potential of Eq. (5) can be calculated analytically. This point is essential to combine the rMUCA sampling with the on-the-fly MLP generation.

To enforce the random walk sampling in the CV subspace, an additional history-dependent potential [13,18,32] is introduced to the Hamiltonian of Eq. (3). The simulated subspace is restricted within the range between c_j^{\min} and c_j^{\max} . The trial configuration during the HMC sweeps is rejected when any of $\{c_j\}$ are out of the range. The history-dependent potential is given by

$$\Delta\delta U(\{c_j\}) = \sum_j [\Delta\delta U_j^0 + k_B T \log h_j(c_j)], \quad (6)$$

where h_j is the histogram for the j th collective variable with a finite bin size. The initial conditions are $\Delta\delta U_j^0 = 0$ and $h_j = 1$. The histogram is updated at each HMC step. The derivative of the histogram potential is evaluated using numerical differentiation. When the highest value of h_j exceeds the criterion $h_{\max} = 1000$, the histogram potential is reset to be $\Delta\delta U_j^0 = \Delta\delta U_j$ and $h_j = 1$.

B. Saddle-point search

Apart from the collection of the training data set for the MLP generation, the decomposed force of Eq. (4) is also useful to search saddle points (transition states). The knowledge of the saddle point enables us to evaluate the reaction rate by assuming the harmonic transition state theory [33]. A first-order saddle point is a stationary point on the potential-energy surface where the Hessian matrix has one and only one negative eigenvalue. If we can choose one CV that characterizes the reaction process properly, the structural relaxation using the following modified force is expected to converge to a transition state,

$$\mathbf{F}_i^*(\{\mathbf{r}_j\}) = \mathbf{F}_i(\{\mathbf{r}_j\}) - (1 + \lambda)\mathbf{F}_i^{\parallel}(\{\mathbf{r}_j\}), \quad (7)$$

where λ is a positive number. By inverting the parallel component of the real force \mathbf{F}_i , the system performs an uphill walk along the potential-energy subspace restricted by the CV and a downhill walk in all other directions. In our experience, $\lambda \simeq 0.5$ is an appropriate choice ($\lambda = 1$ sometimes causes numerical instability).

Several methods have been proposed to find saddle points [34,35], the climbing nudged elastic band (cNEB) method, the dimer method, the Lanczos iterative method, the rational function optimization with approximate Hessian, and

so on. The cNEB method requires the knowledge of the initial and final states and the one-to-one correspondence between constituent atoms of both states. The other methods are the Hessian-based ones in which the minimum eigenmode is evaluated with the exact or approximate Hessian. The advantage of the present method over these existing methods is that no evaluation of the Hessian matrix is required during this saddle-point search. This method also requires no knowledge of the final state of the transition. Once the transition state is obtained, the final state can easily be calculated by searching a nearby local energy-minimum state in the forward direction with the standard structural relaxation method.

C. Machine learning potential

In this section, the formulation of our MLP is described briefly to make this paper self-contained. A monoatomic system is considered here for simplicity. The details of our formulation including the extension to a multiatomic species system can be found in Ref. [24]. The power spectrum of the Fourier coefficients in the spherical coordinates is used as the descriptor to characterize local atomic geometries. The descriptor for the l th atom located at \mathbf{r}_l is given by

$$\mathbf{g}^l = g_{nl}^l = \sum_{m=-l}^l f_{nlm}^l f_{nlm}^l, \quad (8)$$

with the angle-resolved function,

$$f_{nlm}^l = \sum_{i \neq l} f_{\text{cut}}(r_i^l) j_l(q_n r_i^l) Y_{lm}(\hat{\mathbf{r}}_i^l), \quad (9)$$

where $\mathbf{r}_i^l = \mathbf{r}_i - \mathbf{r}_l$, $r_i^l = |\mathbf{r}_i^l|$, j_l 's are the spherical Bessel functions, Y_{lm} 's are the real spherical harmonics, and f_{cut} is a smooth radial cutoff function with the cutoff radius of r_{cut} . The sampling wave-vector lengths are set to be $q_n = 2\pi n/r_{\text{cut}}$. The similarity measure between two local geometries is given by

$$d^2(\mathbf{g}^l, \mathbf{g}^J) = \sum_{n=0}^{n_{\text{max}}} \sum_{l=0}^{l_{\text{max}}} |g_{nl}^l - g_{nl}^J|^2, \quad (10)$$

where the resolution of the descriptors is controlled by n_{max} and l_{max} . Using this similarity measure, the total energy of the system is expressed by a sum of weighted Gaussians,

$$U = \sum_{J \in \text{ref}} \alpha_J \sum_l Q(\mathbf{g}^l, \mathbf{g}^J), \quad (11)$$

where $Q(\mathbf{g}^l, \mathbf{g}^J) = \exp[-d^2(\mathbf{g}^l, \mathbf{g}^J)/(2\theta^2)]$ approximates the overlap between two geometries, α are the regression coefficients, and θ is the scale parameter. The index J runs over the reference descriptors that are selected from the local geometries in the sample data set by the recursive bisection method with the k -means clustering. This treatment removes highly correlated configurations and, thus, enhances the computational efficiency without significant loss of accuracy. The analytical evaluation of the atomic force is straightforward.

For a given sample data set, the squared sum of the residuals of the total energy and force is minimized with the standard L_2 regularization to determine the regression coefficients in Eq. (11). The normalization parameters \mathcal{D} are introduced for

TABLE I. Parameters for MLP construction. The scale parameter θ , regularization parameter λ , descriptor expansion parameters, n_{max} and l_{max} , cutoff radius r_{cut} , normalization parameters \mathcal{D}^{-1} , spilling factor tolerance s_{large} , and recursive bisection criterion δr .

MLP parameters	
θ	0.3
λ	1×10^{-2}
n_{max}	12
l_{max}	6
r_{cut} (bohr)	8.5
$\mathcal{D}_{\text{energy}}^{-1}$ (hartree/atom)	5×10^{-5}
$\mathcal{D}_{\text{force}}^{-1}$ (hartree/bohr)	1×10^{-3}
s_{large}	0.02
δr	0.05

the energy and force to make them dimensionless and treat the quantities with different physical units on the same footing. During the simulation run, the simultaneous error estimation is performed using the following spilling factor,

$$s(\mathbf{g}) = 1 - \sum_{I \in \text{ref}} \sum_{J \in \text{ref}} Q(\mathbf{g}, \mathbf{g}^I) Q^{-1}(\mathbf{g}^I, \mathbf{g}^J) Q(\mathbf{g}^J, \mathbf{g}). \quad (12)$$

This factor becomes zero when the geometry \mathbf{g} is fully projected by the reference descriptors, whereas, $s = 1$ when \mathbf{g} has no overlaps between them. A smaller value of s is expected to result in higher accuracy of the MLP.

The MLP construction is carried out with the following SLAD procedure [18]: (i) During the HMC simulations with the MLP, a sample structure is collected when the maximum value of the spilling factors exceeds the tolerance s_{large} or 2000 HMC steps proceed without any sample collection. Once a sample structure is collected, the HMC simulation is suspended. (ii) The DFT calculation is performed on the new sample structure, and the result is added to the sample data set. (iii) The MLP is reconstructed with the updated sample data set. (iv) The HMC simulation is restarted from the latest accepted configuration. The parameters for the MLP construction used in this paper are summarized in Table I.

D. DFT calculation

The DFT calculations for the collected sample structures are performed using the ultrasoft pseudopotential method [36–38]. The cutoff energies are 15 and 120 hartree for the wave function and charge density, respectively. A Γ -centered $2 \times 2 \times 1$ k -point mesh is used for the Brillouin-zone integration, and Gaussian smearing with a width of 6 mhartree is applied.

Long-range van der Waals (vdW) forces play an important role for surface reactions. The local-density approximation [39–41] and semilocal generalized gradient approximation (GGA) [42–44], which are commonly adopted for the exchange-correlation functional in DFT calculations, cannot describe this interaction properly. In order to deal with the vdW interaction accurately, the nonlocal correlation energy, optB86b-vdW [45], is adopted for the exchange-correlation energy. It was shown that this functional correctly describes the site preference of CO on the Pt(111) surface [46]. Double spatial

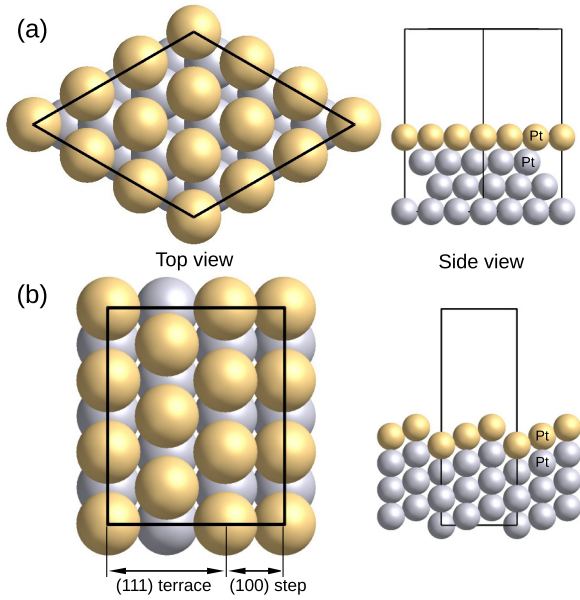


FIG. 1. Slab models for (a) Pt(111) and (b) Pt(211) surfaces. Computational unit cells are represented by thick lines. Pt atoms in the top surface layer are depicted in light yellow, and others are depicted in silver. The same color scheme is used in the subsequent figures.

integrals for the nonlocal functional are carried out using the interpolation scheme [47,48].

The DFT code as well as the machine learning code used in this paper have been developed by the author and already applied successfully to a wide variety of the systems [18,24,26–29,37,38,48–52].

III. RESULTS AND DISCUSSION

A. MLP construction

The rMUCA ensemble method is applied to the CO oxidation reaction on Pt surfaces. Two kinds of surfaces Pt(111) and Pt(211) are considered. The Pt(111) surface shows an ideal flat terrace, whereas the Pt(211) surface is a stepped one and consists of three-atom-wide (111) terraces and (100) step edges. These surfaces are simulated by repeated slab models which are shown in Fig. 1. The slab models are constructed using the theoretical bulk lattice constant, $a = 3.950$ Å, that is in good agreement with the experimental value of 3.925 Å [53]. The periodicity in the lateral directions is set to be $p(3 \times 3)$ and $p(3 \times 1)$ for Pt(111) and Pt(211), respectively. Both slab models are composed of four Pt layers with a 10-Å vacuum. To simulate the CO oxidation reaction, one CO molecule and one O adatom are placed on the top surface of the Pt slab. The corresponding coverage of CO and O is 1/9 monolayers for both Pt(111) and Pt(211). These two slab models are used throughout this paper. In the HMC simulations, the harmonic well potential is additionally applied to the bottom two Pt layers in order to simulate the bulk crystal, $V_{\text{well}} = \frac{k}{2} \sum_i |r_i - r_i^b|^2$, where r_i^b 's denote bulk Pt positions, and the spring constant is set to $k = 0.1$ hartree/bohr².

For the rMUCA sampling, the C-O coordination number is chosen as the CV, which is calculated from the

expression [54],

$$CN = \sum_i \frac{1 - \left(\frac{\Delta r_i}{d}\right)^6}{1 - \left(\frac{\Delta r_i}{d}\right)^{12}}, \quad (13)$$

where Δr_i 's are the interatomic distances between C and O atoms, the scale parameter is $d = 1.46$ Å, and i runs over two O atoms in the C-centered Wigner-Seitz cell. The CV range from 1 to 2 is discretized with 20 bins. This CV choice allows us equivalent treatment for two types of oxygen atoms, an oxygen adatom on the surface and O in the CO molecule, and, thus, the exchange between them via the oxidation and subsequent reduction reactions is naturally incorporated into the simulation. The unfavorable CO dissociation can be prevented by setting the CV range to be from 1 to 2.

First, two MLPs are generated for the Pt(111) and Pt(211) surfaces, separately. The HMC simulations are carried out at $T = 500$ K and the simulation period is taken to be 200 000 HMC steps. Three MD steps with a time-step size of 0.97 fs are used for the configuration updates. The sample structures for training are collected by the SLAD approach. As the initial configuration for the Pt(111) surface, a CO molecule is placed at the top site, and an oxygen adatom O* is placed at the hollow-hcp site: Hereafter, the O adatom is denoted as O* to distinguish it from O in the CO molecule. For the Pt(211) surface, CO and O* are placed at the top and hollow-fcc sites on the (111) terrace, respectively.

Figure 2 depicts the profiles of the CV, the C-O coordination number, during the HMC simulations with the rMUCA sampling. The CV exhibits rapid oscillations over the range from 1 to 2 both for Pt(111) and Pt(211), indicating the promotion of the reaction, $\text{CO} + \text{O}^* \leftrightarrow \text{CO}_2$. This can be confirmed visually from the snapshots shown in Fig. 2. The number of the sample structures collected by the SLAD, on which the DFT calculations are performed, is 178 and 195 for Pt(111) and Pt(211), respectively. Since each HMC simulation includes about 600 000 configuration updates, the structure sampling is considerably accelerated by the dynamical data collection with the SLAD.

Then, the MLP is reconstructed using both sample data sets collected for Pt(111) and Pt(211). Total number of the sample structures is 373, which contain 14 547 local atomic geometries. Applying the recursive bisection method for sparsification [24], the number of the regression coefficients is reduced to 5398. Figure 3 shows the scatter plots for the reconstructed MLP where 40 test configurations are taken from two HMC runs every 10 000 steps. The MLP reproduces the DFT results quite well. The mean absolute errors for the test (training) data set are 1.2×10^{-4} (7.7×10^{-5}) hartree/atom and 3.1×10^{-3} (2.5×10^{-3}) hartree/bohr for the total energy and force, respectively. The small differences between the prediction errors for the training and test datasets indicate that the physically relevant configuration subspace is suitably covered with the sample structures collected by the SLAD.

If only the history-dependent potential is used as the bias potential, which corresponds to the metadynamics [31], it also promotes the oscillations of the CV. The periods of the oscillations, however, become somewhat longer than those with the rMUCA bias potential. The rMUCA method enhances the random walk in the subspace restricted by the CVs and

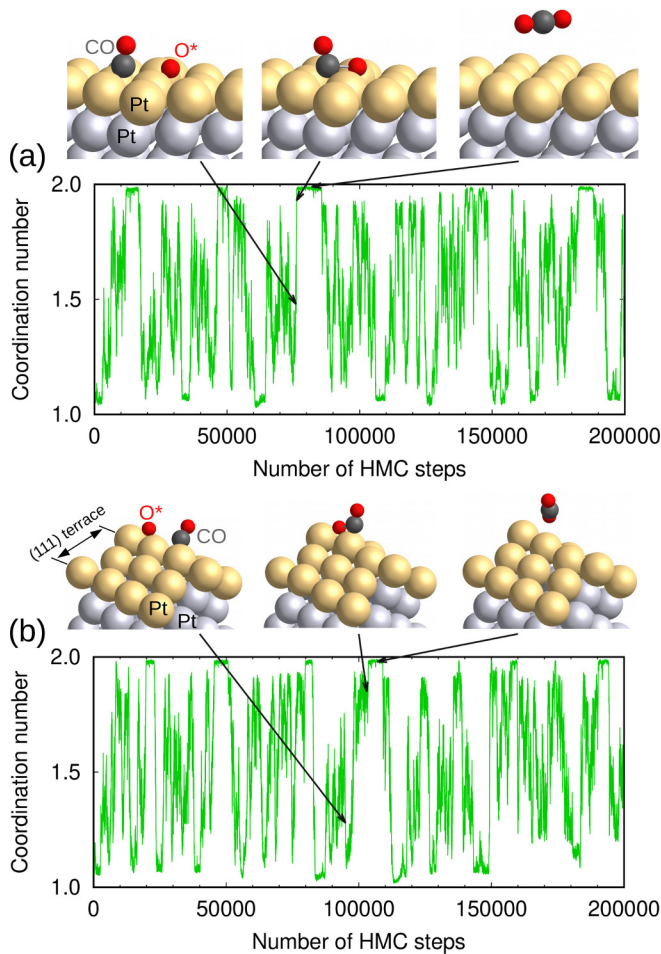


FIG. 2. Profiles of the CV (the C-O coordination number) during the HMC simulations with the rMUCa ensemble, together with selected snapshots of the geometries. (a) Pt(111) and (b) Pt(211).

allows us efficient sampling of rare events. The disadvantage of the rMUCa sampling is that the history-dependent potential obtained by it does not correspond to the free-energy surface as a function of the CV. The recalculation with the metadynamics is, however, relatively easy if the well-trained MLP is constructed with the rMUCa sampling.

B. MD simulation

Using the constructed MLP, the conventional NVT MD simulations are carried out for the Pt(111) and Pt(211) surfaces with CO and O^* adsorbates. The potential V_{well} is added for the bottom two Pt layers as performed in the HMC simulations with the rMUCa sampling. The Noé-Poincaré thermostat [10] is used to control temperature at $T = 500$ K. The simulation period is taken to be 200 000 MD steps with a time-step size of 1.94 fs. During MD runs for both surfaces, the maximum values of the spilling factor are kept smaller than the tolerance ($s_{\text{large}} = 0.02$), suggesting high accuracy of the simulations (see the left insets of Fig. 4).

Trajectories of C and O^* are shown in Fig. 4 where the trajectory of O in the CO molecule is not shown for clarity since no breaking of the C-O bond is observed in both simulations. For the Pt(111) surface, the simulation starts with CO at

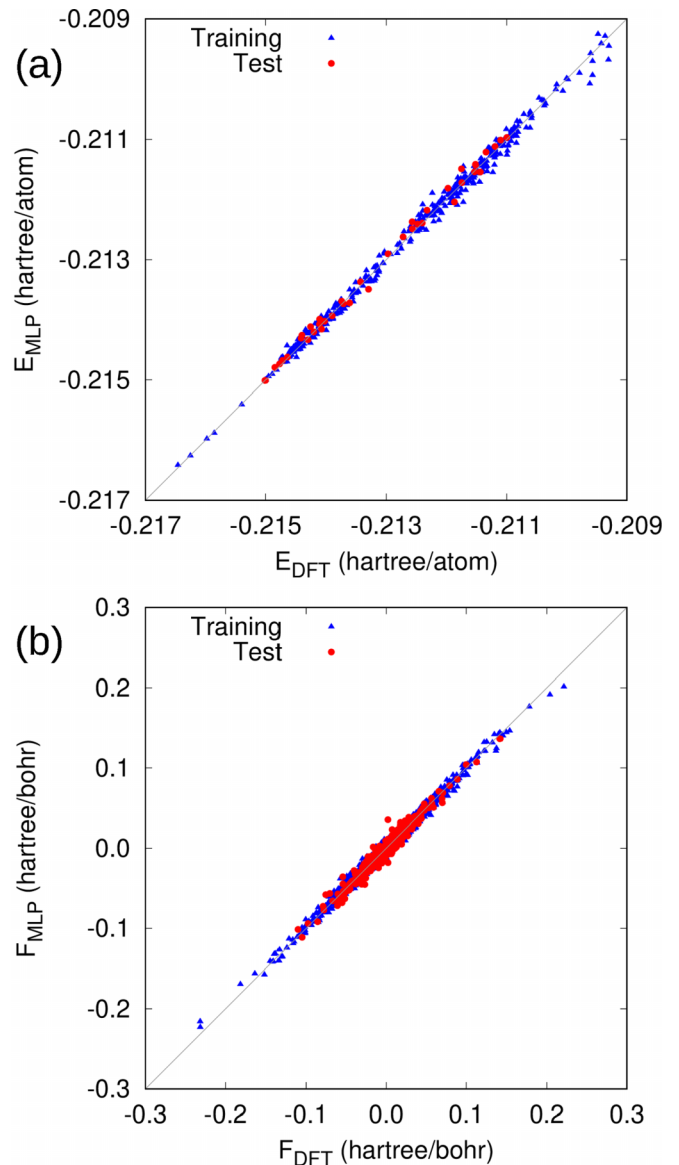


FIG. 3. Scatter plots for (a) total energy and (b) force.

the top site and O^* at the hollow-hcp site. It is found that O^* is not diffusive and fluctuates around the hollow-hcp site. On the other hand, the CO molecule shows surface diffusion via the bridge and hollow sites, but does not approach the O^* site. This implies the repulsive interaction between CO and O^* .

In the starting configuration for the Pt(211) surface, CO and O^* are placed at the top and hollow-fcc sites on the (111) terrace, respectively. After about 3000 MD steps, O^* hops to the bridge site on the step edge and is trapped there for the rest of the simulation period. The CO molecule also prefers the step edge and is mainly located at the top site on it. The reason for the preferential occupation of the sites on the step edge is probably due to the low coordination number of Pt on the step edge, which will make these Pt atoms chemically reactive [55,56].

The profiles of the C-O coordination number during the MD runs are given in the right insets of Fig. 4. The variations in the coordination number do not cover the entire range

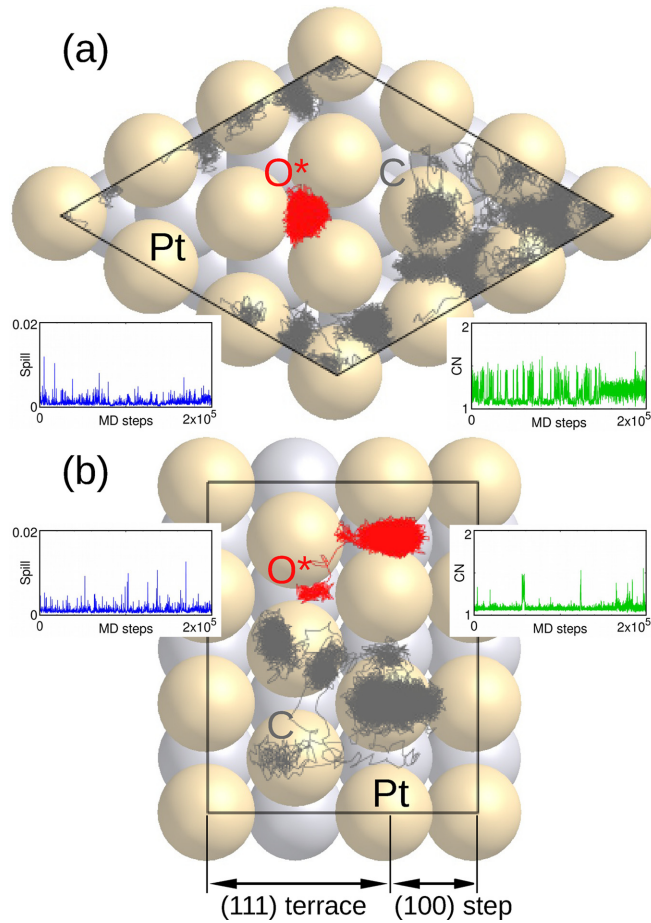


FIG. 4. Trajectories of C and O* calculated with conventional MD simulations at $T = 500$ K. (a) Pt(111) and (b) Pt(211). The profiles of the maximum spilling factor and the C-O coordination number are given in the left and right insets, respectively.

from 1 to 2 and are limited within the region of $CN \lesssim 1.5$, indicating that no formations of CO_2 are reproduced in the MD simulations. Comparing these profiles with those shown in Fig. 2, we can confirm that the rMUCA sampling allows us efficient collection of rare-event configurations that are difficult to access in the physical ensemble simulations.

C. CO oxidation reaction

The energetics and reaction pathways of the CO oxidation reactions on the Pt(111) and Pt(211) surfaces are investigated using the MLP. For Pt(111), CO at the bridge site and O* at the hollow-hcp site are chosen as the initial state (IS), which is found to be the most stable configuration in the present coverage. According to the result of the standard MD simulation, two adsorbates located on the step edge are chosen as the IS for Pt(211) where CO and O* are placed at the top and bridge sites, respectively. The standard structural relaxation is performed for them. Then, the uphill relaxation with the modified force of Eq. (7) is applied to the IS to find the transition state (TS). The final state (FS) is obtained by applying the subsequent standard downhill relaxation to the TS. At the beginning of the uphill and downhill relaxation, the interatomic distance between C and O* is shortened by

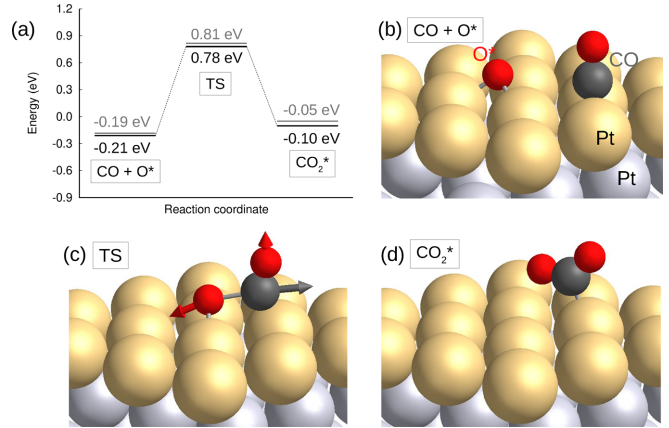


FIG. 5. Energetics of the CO oxidation reaction on the Pt(111) surface. (a) Energy diagram, where the black (gray) lines represent the MLP (DFT) results. The geometries of (b) the initial state ($\text{CO} + \text{O}^*$), (c) the TS, and (d) the final state (CO_2^*). The arrows in (c) show the eigenvector of the minimum eigenmode where the Pt components are omitted because of their negligible contribution.

about 0.5 \AA to create nonzero terms in the force. During the relaxation processes, the bottom two layers of the Pt slabs are fixed at their bulk positions. In this section, the origin of the energy is set to be the sum of the total energies of the clean Pt surface and an isolated CO_2 molecule calculated by DFT where the latter is calculated using a face-centered cubic supercell with the lattice constant of $a = 16 \text{ \AA}$. Figure 5 shows the result for the Pt(111) surface. The energy barrier in the forward direction (the energy difference between the IS and TS) is predicted to be $\Delta E = 0.99 \text{ eV}$. This agrees well with the previous theoretical result obtained by the DFT-GGA calculation, 1.05 eV [57]. The interatomic distance between C and O* in the TS is $d_{\text{CO}^*} = 1.88 \text{ \AA}$ that is about 1.6 times longer than the theoretical C-O bond length in the isolated CO_2 molecule (1.19 \AA). The FS is obtained to be a bent-shaped CO_2^* complex (an asterisk is introduced to denote a chemisorbed state of CO_2) which is weakly bound on the Pt(111) surface with the adsorption energy $E = -0.10 \text{ eV}$. The C-O bond lengths of CO_2^* are $d_{\text{CO}_2^*} = 1.23, 1.28 \text{ \AA}$ which are slightly longer than that in the CO_2 molecule and the O-C-O bond angle is $\theta_{\text{CO}_2^*} = 132.7^\circ$. It is confirmed that the Hessian matrices for the IS and FS have no negative eigenvalues, and that for the TS has only one negative eigenvalue. The eigenvector of the minimum eigenmode in the TS gives the reaction coordinate at the saddle point, which is shown in Fig. 5(c). The corresponding vibrational frequency is $\nu^\# = 346i \text{ cm}^{-1}$. To check the robustness of the saddle-point search method, the uphill relaxation is repeated using the C-O* interatomic distance as the CV. The obtained geometric parameter and the energy of the TS are essentially the same as those calculated with the CN, indicating that the present method is almost unaffected by the choice of the CV.

The result for the Pt(211) surface is shown in Fig. 6. The geometries of the CO-O* complexes obtained for the TS and FS are relatively similar to those on Pt(111). For the TS, the C-O* distance is $d_{\text{CO}^*} = 1.96 \text{ \AA}$. A bend-shaped CO_2^* complex is also found as the FS of Pt(211) in which $d_{\text{CO}_2^*} = 1.23, 1.25 \text{ \AA}$ and $\theta_{\text{CO}_2^*} = 144.7^\circ$. By checking the eigenvalues of the

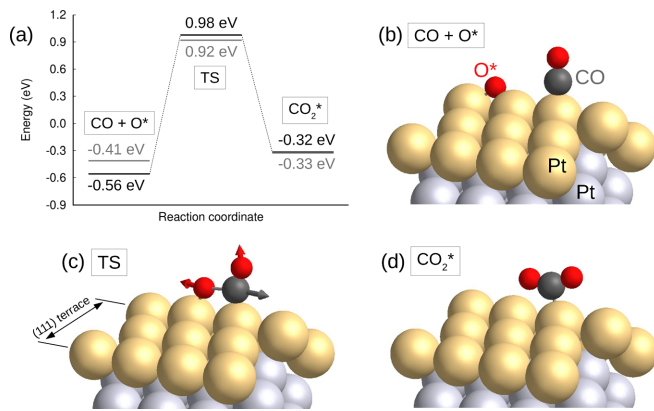


FIG. 6. Energetics of the CO oxidation reaction on the Pt(211) surface. See the caption of Fig. 5.

Hessian matrices, it is identified that IS and FS are local energy minima, and TS is a first-order saddle point. The imaginary vibrational frequency in TS is $\nu^\# = 381i \text{ cm}^{-1}$. The energies of the IS and FS are lower than those of Pt(111) by 0.35 and 0.22 eV, respectively, most likely owing to high reactivity of the Pt atoms on the step edge as mentioned in the previous section. The previous DFT calculation with GGA [56] also supports more stable adsorption of CO and CO_2^* at the step edge than at the flat terrace. If the reactants become more stable, in general, the reaction among them is accompanied with a higher-energy barrier because of the high-energy cost for breaking/reforming of their bonds. In fact, the barrier height is predicted to be $\Delta E = 1.53 \text{ eV}$ which is 0.54 eV higher than that of Pt(111).

Assuming the harmonic transition state theory [33], the reaction rate coefficients at 500 K are estimated to be 4.1×10^2 and $4.7 \times 10^{-3} \text{ s}^{-1}$ for Pt(111) and Pt(211), respectively. The coefficient of Pt(211) is five orders of magnitude smaller than that of Pt(111). The stable adsorbates on the step edge cause a higher-energy barrier. Thus, the stepped Pt surfaces are expected to inhibit the CO oxidation, at least, for low coverage surfaces where the adsorption of CO and O^* on the step edge will be dominate [58,59].

Finally, the DFT total-energy calculations are performed on the IS, TS, and FS configurations obtained by the MLP. These results are also given in Figs. 5(a) and 6(a). As can be seen, the deviations of the MLP energies from the DFT ones are kept small: They are less than 0.1 eV in most cases, and the only exception is 0.15 eV for the IS of Pt(211). These errors do not affect our consideration for the characteristic of the CO oxidation reaction on the Pt surfaces discussed in this section.

The MLP generated with the on-the-fly rMUCA sampling shows sufficient accuracy to simulate the chemical reactions involving the transitions between the states separated by energy barriers.

IV. SUMMARY

In this paper, the restricted multicanonical ensemble method was combined with the on-the-fly MLP generation scheme, SLAD. The rMUCA simulation performed a random walk in the potential-energy subspace restricted by the selected collective variables. Any preliminary simulation runs were not required to construct a bias potential. This feature was essential to apply the rMUCA simulation to the on-the-fly MLP generation. The rMUCA formula can be easily modified for the saddle-point search.

The utility of the method was demonstrated for the CO oxidation reactions on the Pt surfaces. Two kinds of the surfaces, flat Pt(111) and stepped Pt(211), were considered. The rMUCA simulations successfully promoted the CO oxidation reaction which was difficult to reproduce in the standard ensemble simulations. During about 1 200 000 configuration updates in the HMC sweeps, the total number of the DFT calculations required is only 373, indicating remarkable efficiency of the dynamical data collection with the SLAD. The constructed MLP shows sufficient accuracy to predict the energetics of the CO oxidation reactions in which the validity of the saddle-point search scheme using the rMUCA formula is also confirmed. The rMUCA simulation combined with the SLAD provides an efficient and accurate way to generate the MLP applicable to the rare events. From an application point of view, the present results suggest that step edges on the Pt surfaces inhibit the CO oxidation.

In the rMUCA simulation, the choice of collective coordinates is a critical step, which depends on the system of interest. Although a universal recipe has not yet been proposed, we can find a large variety of examples in the published metadynamics papers [54,60–62]. The several useful guidelines have also been suggested to generate appropriate CVs [31]. In this context, the similarity measure for the MLP descriptors given in Eq. (10) is expected to be a good CV in many cases since it accurately characterizes the local atomic environment.

ACKNOWLEDGMENTS

I thank R. Jinnouchi for useful discussions.

[1] M. E. Tuckerman and G. J. Martyna, *J. Phys. Chem. B* **104**, 159 (2000).
 [2] D. P. Landau and K. Binder, *A Guide to Monte Carlo Simulations in Statistical Physics*, 4th ed. (Cambridge University Press, Cambridge, UK, 2014).
 [3] N. Metropolis, A. W. Rosenbluth, M. N. Rosenbluth, A. H. Teller, and E. Teller, *J. Chem. Phys.* **21**, 1087 (1953).
 [4] I. McDonald, *Mol. Phys.* **23**, 41 (1972).

[5] H. C. Andersen, *J. Chem. Phys.* **72**, 2384 (1980).
 [6] M. Parrinello and A. Rahman, *Phys. Rev. Lett.* **45**, 1196 (1980).
 [7] S. Nosé, *Mol. Phys.* **52**, 255 (1984).
 [8] W. G. Hoover, *Phys. Rev. A* **31**, 1695 (1985).
 [9] R. M. Wentzcovitch, *Phys. Rev. B* **44**, 2358 (1991).
 [10] S. Nosé, *J. Phys. Soc. Jpn.* **70**, 75 (2001).
 [11] A. M. Ferrenberg and R. H. Swendsen, *Phys. Rev. Lett.* **61**, 2635 (1988).

- [12] B. A. Berg and T. Neuhaus, *Phys. Rev. Lett.* **68**, 9 (1992).
- [13] F. Wang and D. P. Landau, *Phys. Rev. Lett.* **86**, 2050 (2001).
- [14] M. S. Shell, P. G. Debenedetti, and A. Z. Panagiotopoulos, *Phys. Rev. E* **66**, 056703 (2002).
- [15] H. Okumura and Y. Okamoto, *Phys. Rev. E* **70**, 026702 (2004).
- [16] H. Okumura, *J. Phys. Soc. Jpn.* **81**, SA001 (2012).
- [17] P. M. Piaggi and M. Parrinello, *Phys. Rev. Lett.* **122**, 050601 (2019).
- [18] K. Miwa, *Phys. Rev. B* **103**, 144106 (2021).
- [19] P. Hohenberg and W. Kohn, *Phys. Rev.* **136**, B864 (1964).
- [20] W. Kohn and L. J. Sham, *Phys. Rev.* **140**, A1133 (1965).
- [21] R. O. Jones, *Rev. Mod. Phys.* **87**, 897 (2015).
- [22] J. Behler and M. Parrinello, *Phys. Rev. Lett.* **98**, 146401 (2007).
- [23] A. P. Bartók, M. C. Payne, R. Kondor, and G. Csányi, *Phys. Rev. Lett.* **104**, 136403 (2010).
- [24] K. Miwa and H. Ohno, *Phys. Rev. B* **94**, 184109 (2016).
- [25] R. Jinnouchi, K. Miwa, F. Karsai, G. Kresse, and R. Asahi, *J. Phys. Chem. Lett.* **11**, 6946 (2020).
- [26] K. Miwa and H. Ohno, *Phys. Rev. Mater.* **1**, 053801 (2017).
- [27] K. Miwa and R. Asahi, *Phys. Rev. Mater.* **2**, 105404 (2018).
- [28] K. Miwa and R. Asahi, *Int. J. Hydrogen Energy* **44**, 23708 (2019).
- [29] K. Miwa and R. Asahi, *Solid State Ion.* **361**, 115567 (2021).
- [30] B. Mehlis, D. W. Heermann, and B. M. Forrest, *Phys. Rev. B* **45**, 679 (1992).
- [31] A. Barducci, M. Bonomi, and M. Parrinello, *WIREs Comput. Mol. Sci.* **1**, 826 (2011).
- [32] U. H. E. Hansmann and L. T. Wille, *Phys. Rev. Lett.* **88**, 068105 (2002).
- [33] G. Henkelman, G. Jóhannesson, and H. Jónsson, in *Theoretical Methods in Condensed Phase Chemistry*, edited by S. D. Schwartz (Springer, Dordrecht, 2002), pp. 269–302.
- [34] G. Henkelman, B. P. Uberuaga, and H. Jónsson, *J. Chem. Phys.* **113**, 9901 (2000).
- [35] R. A. Olsen, G. J. Kroes, G. Henkelman, A. Arnaldsson, and H. Jónsson, *J. Chem. Phys.* **121**, 9776 (2004).
- [36] D. Vanderbilt, *Phys. Rev. B* **41**, 7892 (1990).
- [37] K. Miwa, *Phys. Rev. B* **84**, 094304 (2011).
- [38] K. Miwa, *Phys. Rev. B* **97**, 075143 (2018).
- [39] E. Wigner, *Phys. Rev.* **46**, 1002 (1934).
- [40] J. P. Perdew and A. Zunger, *Phys. Rev. B* **23**, 5048 (1981).
- [41] J. P. Perdew and Y. Wang, *Phys. Rev. B* **45**, 13244 (1992).
- [42] J. P. Perdew, J. A. Chevary, S. H. Vosko, K. A. Jackson, M. R. Pederson, D. J. Singh, and C. Fiolhais, *Phys. Rev. B* **46**, 6671 (1992).
- [43] J. P. Perdew, K. Burke, and M. Ernzerhof, *Phys. Rev. Lett.* **77**, 3865 (1996).
- [44] Z. Wu and R. E. Cohen, *Phys. Rev. B* **73**, 235116 (2006).
- [45] J. Klimeš, D. R. Bowler, and A. Michaelides, *Phys. Rev. B* **83**, 195131 (2011).
- [46] G. T. K. Kalhara Gunasooriya and M. Saeys, *ACS Catal.* **8**, 3770 (2018).
- [47] J. Wu and F. Gygi, *J. Chem. Phys.* **136**, 224107 (2012).
- [48] K. Miwa, *Phys. Rev. B* **105**, 024109 (2022).
- [49] K. Miwa, S. Takagi, M. Matsuo, and S. Orimo, *J. Phys. Chem. C* **117**, 8014 (2013).
- [50] K. Miwa, T. Sato, M. Matsuo, K. Ikeda, T. Otomo, S. Deledda, B. C. Hauback, G. Li, S. Takagi, and S. Orimo, *J. Phys. Chem. C* **120**, 5926 (2016).
- [51] K. Miwa and R. Asahi, *Phys. Rev. B* **102**, 174313 (2020).
- [52] A. Beniya, K. Miwa, H. Hirata, Y. Watanabe, and S. Higashi, *ACS Catal.* **12**, 1977 (2022).
- [53] H. Ebert, J. Abart, and J. Voithländer, *Z. Phys. Chem.* **144**, 223 (1985).
- [54] M. Iannuzzi, A. Laio, and M. Parrinello, *Phys. Rev. Lett.* **90**, 238302 (2003).
- [55] H. Orita and Y. Inada, *J. Phys. Chem. B* **109**, 22469 (2005).
- [56] L. Zhou, A. Kandratsenka, C. T. Campbell, A. M. Wodtke, and H. Guo, *Angew. Chem. Int. Ed.* **58**, 6916 (2019).
- [57] A. Alavi, P. Hu, T. Deutsch, P. L. Silvestrelli, and J. Hutter, *Phys. Rev. Lett.* **80**, 3650 (1998).
- [58] A. Szabó, Jr., M. A. Henderson, and J. T. Yates, Jr., *J. Chem. Phys.* **96**, 6191 (1992).
- [59] J. Xu, Jr. and J. T. Yates, Jr., *J. Chem. Phys.* **99**, 725 (1993).
- [60] M. Sega, E. Autieri, and F. Pederiva, *J. Chem. Phys.* **130**, 225102 (2009).
- [61] F. Pietrucci and A. Laio, *J. Chem. Theory Comput.* **5**, 2197 (2009).
- [62] S. Angioletti-Uberti, M. Ceriotti, P. D. Lee, and M. W. Finnis, *Phys. Rev. B* **81**, 125416 (2010).